Synchrotron inline phase contrast μCT enables detailed virtual histology of embedded soft-tissue samples with and without staining

Mara Saccomano,[a]‡ Jonas Albers,[a,b]‡ Giuliana Tromba,[c] Marina Dobrivojević Radmilović,[d] Srećko Gajović,[d] Frauke Alves[a,b,e]§ and Christian Dullin[a,b,c]*§

[a]Translational Molecular Imaging, Max Planck Institute for Experimental Medicine, Germany, [b]Institute for Diagnostic and Interventional Radiology, University Medical Center Göttingen, Germany, [c]Elettra-Sincrotrone, Trieste, Italy, [d]Croatian Institute for Brain Research, University of Zagreb School of Medicine, Zagreb, Croatia, and [e]Clinic for Heamatology and Medical Oncology, University Medical Center Göttingen, Germany. *Correspondence e-mail: christian.dullin@elettra.eu

Synchrotron radiation micro-computed tomography (SRμCT) based virtual histology, in combination with dedicated ex vivo staining protocols and/or phase contrast, is an emerging technology that makes use of three-dimensional images to provide novel insights into the structure of tissue samples at microscopic resolution with short acquisition times of the order of minutes or seconds. However, the high radiation dose creates special demands on sample preparation and staining. As a result of the lack of specific staining in virtual histology, it can supplement but not replace classical histology. Therefore, the aim of this study was to establish and compare optimized ex vivo staining and acquisition protocols for SRμCT-based virtual histology of soft-tissue samples, which could be integrated into the standard workflow of classical histology. The high grade of coherence of synchrotron radiation allows the application of propagation-based phase contrast imaging (PBI). In this study, PBI yielded a strong increase in image quality even at lower radiation doses and consequently prevented any damage to the tissue samples or the embedding material. This work has demonstrated that the improvement in contrast-to-noise ratio by PBI enabled label-free virtual histology of soft-tissue specimens embedded in paraffin to a level of detail that exceeds that achieved with staining protocols.

1. Introduction

Classical histology of tissue sections in combination with chemical staining and/or immunohistochemistry (IHC) is widely used in both preclinical research and clinical routine in order to study tissue samples at a cellular level. Over the years, a variety of tissue-specific staining methods have been established, allowing a precise delineation of different morphological structures (Kienan, 2008). However, the main limitation of traditional histology is its two-dimensional nature and the destruction of the sample during the course of the procedure. Indeed, serial sectioning can be performed to assess the sample in three dimensions, but this approach is very labor intensive and the fusion of several sections into a three-dimensional volume data set has to deal with artefacts caused by the cutting process (Ourselin et al., 2001; Handschuh et al., 2010). Alternatively, three-dimensional visualization of thicker biological samples can be obtained for instance by confocal or multiphoton microscopic techniques, but only with very low penetration depth (<1 mm), or with scanning and transmission electron microscopy, which does offer high-resolution three-dimensional imaging but only of very thin samples or close to the cutting edge.
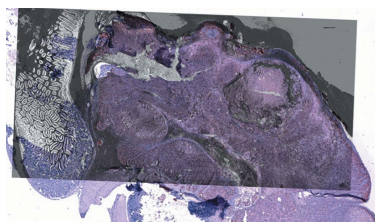
More recently, light sheet fluorescence microscopy has been used to perform fast volumetric imaging of intact organs, embryos and organisms, but this technique allows visualization of fluorophores only after optical clearance of the specimen (Tomer *et al.*, 2015). In addition, micro-molecular resonance imaging (μMRI) can also provide three-dimensional visualization of soft-tissue specimens but only with limited spatial resolution and at high experimental costs (Li *et al.*, 2007; Duce *et al.*, 2011; Liu *et al.*, 2010).

Virtual histology based on micro-computed tomography (μCT) is an emerging technology that provides three-dimensional visualization of different features of soft-tissue specimens, such as the structure of the intrahepatic biliary system (Masyuk *et al.*, 2001) and of lung tissue (Kitchen *et al.*, 2005), medulloblastoma formation (Prajapati *et al.*, 2011) and even the development of embryos (Johnson *et al.*, 2006), which can be virtually sliced at any point and in any direction. Although the spatial resolution in the micrometer range allows the characterization of anatomical structures within the specimen without destroying it (Schulz *et al.*, 2010; Zehbe *et al.*, 2010), visualization of soft tissue, especially in very small specimens such as murine organs, remains a challenge because of the low contrast resolution (Clark & Badea, 2014).

Therefore, staining procedures based on heavy ions (Metscher, 2009*a*,*b*; Dullin *et al.*, 2017; Missbach-Guentner *et al.*, 2018) and the application of special phase-retrieval algorithms have been generated in order to improve the signal-to-noise ratio (SNR) of the tomographic images. We have already demonstrated that CT-staining procedures, such as the use of photo-tungstic acid (PTA), neither introduce morphological tissue alterations, such as tissue damaging, nor molecular or chemical modifications, such as the loss of intracellular/plasmalemmal markers or alterations of tissue charge, respectively. Thus, they can be subsequently combined with classical histology and IHC (Dullin *et al.*, 2017).

Alternatively, high-resolution imaging of non-mineralized (soft) tissues in the sub-micrometer range can be provided by synchrotron radiation micro-computed tomography (SRμCT) (Mohammadi *et al.*, 2014) as a result of the high flux that allows the use of detectors with very small pixel sizes at low total scanning times of seconds or minutes. The small X-ray focal spot and the large source-to-sample distance facilitate the use of phase contrast but provide only small cone-angles and hence a rather limited field of view compared with classical μCT.

Here we present and compare different adapted staining and imaging protocols for SRμCT-based virtual histology. We demonstrate that the combination of high X-ray flux and increased absorption of the sample, attributed to the applied staining, leads to the deposition of large radiation doses within the sample, resulting in increased deterioration of the embedding material. This can subsequently lead to a low image quality, because of induced local movement of the sample, as well as artifacts in the virtual histology analysis. Possible damage of the tissue cannot be ruled out, but has not been observed so far during the histological analysis of the scanned sample. Moreover, the three-dimensional visualization of multiple types of soft-tissue such as lung, heart, brain and pancreatic tumors was obtained with such high resolution to perfectly distinguish anatomical structures in the range of sub-micrometers. Most importantly, we confirmed that this method does not interfere with subsequently performed classical histological analysis. Moreover, by applying PBI we achieved a dramatic reduction of the radiation dose and thereby minimized the deterioration of the embedding material. The improved soft-tissue contrast by PBI even allowed label-free virtual histology of unstained soft-tissue samples which has a high potential for clinical translation.

2. Materials and methods

2.1. Biological samples

Organs such as hearts, lungs and brains were isolated from adult inbred C57BL6 mice. Human pancreatic tumor xenografts were obtained from male athymic nude mice NMRI-Foxn1nu (Charles River Laboratories) four weeks after orthotopic transplantation of 1×10^6 AsPC-1 human pancreatic ductal adenocarcinoma (PDAC) cells into the head of the pancreas as described previously (Saccomano *et al.*, 2016). All animal procedures were performed in accordance with European guidelines (2010/63/EU) and approved by the corresponding ethics institutions (administration of Lower Saxony, Germany, license No. 33.9-42502-04-13/1085 and Ministry of Agriculture of Croatia No. UP/I-322-01/14-01/128).

2.2. Adapted soft-tissue staining protocols for SRμCT

Three different staining protocols based on phospho-tungstic acid (PTA; Sigma Aldrich), iodine (I_2; Sigma Aldrich) and chrome alum [chromium(III) potassium sulfate; Morphisto] were applied and optimized for SRμCT.

For PTA staining, isolated mouse organs [hearts ($N = 2$), lungs ($N = 2$), brains ($N = 2$)] and AsPC-1 tumors ($N = 4$) were washed once with PBS and dehydrated directly with 35% and 75% ethanol for 1 h each. After the dehydration process, organs were stained with a solution containing 0.7% PTA, 4% PFA and 70% ethanol. The staining time varied according to the size and hardness of the sample, ranging between overnight (O/N) for small and soft samples such as heart and lungs, and 10 days for compact organs of greater size such as brain and tumor. Then, samples were washed with 75% ethanol and dehydrated with 75%, 95% and 100% ethanol for 3 h each (see Table 1).

Adapting a previously published I_2 staining protocol (Metscher, 2009*a*,*b*), isolated organs ($N = 2$ hearts, lungs and brains) were briefly washed with phosphate buffered saline (PBS) and fixed O/N with 4% paraformaldehyde (PFA; Serva Electrophoresis) at room temperature (RT). Samples were then dehydrated gradually with 60% and 75% of ethanol for 1.5 h each, with 100% ethanol for 4 h and stained O/N with 1% I_2 diluted in 100% ethanol. Before embedding, stained samples were washed once in 100% ethanol (see Table 1).

Table 1
Summary of staining protocols, samples and SRμCT settings used.

		Phosphotungstic acid (PTA)	Iodine (I₂)	Chrome alum	No staining
Protocol	1. Fixation	None	1 × wash with PBS, 4% PFA O/N at RT	1 × wash with PBS, 4% PFA O/N at RT	1 × wash with PBS, 4% PFA O/N at RT
	2. Dehydration	1 × wash with PBS, 35%, 75% ethanol (1 h each)	60%, 75% ethanol (1.5 h each) and 100% ethanol (4 h)	None	None
	3. Staining	Staining solution: 0.7% PTA, 4% PFA and 70% ethanol	1% I₂ diluted in 100% ethanol	Gallocyanin chrome alum staining solution diluted 1:1 in water	None
	4. Dehydration	1 × wash with water, 75%, 95%, 100% ethanol (3 h each)	1 × wash with 100% ethanol	1 × wash with water, 60%, 75%, 95%, 100% ethanol (3 h each)	1 × wash with water, 60%, 75%, 95%, 100% ethanol (3 h each)
	5. Embedding	Xylol (3 h), paraffin/agarose	Xylol (1.5 h), paraffin/agarose	Xylol (3 h), paraffin/agarose	Xylol (3 h), paraffin
	Duration of the staining	O/N at RT (heart and lung) 10 days (brain and AsPC-1 tumor)	O/N at RT	O/N at RT	–
Samples		Heart, lung, brain, AsPC-1 tumor	Heart, lung, brain	Heart, lung, brain	Brain
SRμCT settings	X-ray average energy (after filtering)		19–22 keV		
	Sample-to-detector distance		10 cm		
	Rotation angle		360°, off-center		
	Projections	900 (heart for the CNR experiment) 1800 (lung, heart, brain)	1800		1800
	Exposure time per projection(s)	2 s (AsPC-1 tumor) 100 ms (lung, heart, brain) 1 s, 500 ms, 250 ms, 125 ms, 62.5 ms (heart for the CNR experiment)	50 ms		100 ms
	Filter	1 mm aluminium + 1 mm silica (AsPC-1 tumor) 1 mm silica (heart, lung, brain)	1 mm silica	1 mm silica	1 mm silica
	Voxel size (μm³)	2.6	2	2.6	2
	Total acquisition time		1 h for high dose protocol 45 s for the low dose protocol		

For the modification of a chrome alum based staining method (Metscher, 2009*a*,*b*), isolated organs ($N = 2$ hearts, lungs and brains) were briefly washed with PBS, fixed O/N with 4% PFA and stained O/N with the gallocyanin chrome alum staining solution diluted 1:1 in water. Before embedding, organs were extensively washed in water and dehydrated with 60%, 75%, 95% and 100% ethanol for 3 h each (see Table 1).

The unstained brains ($N = 2$) were washed in PBS after fixation, followed by the dehydration process in ascending concentrations of ethanol before paraffin embedding (Table 1).

2.3. Embedding, sectioning and histology of tissue samples

After staining, tissue samples were either transferred to a Xylol solution (Merck) for either 1.5 h (I₂ staining) or 3 h (chrome alum and PTA staining), which serves as a transition medium between the dehydrating ethanol solutions and the paraffin embedding, or they were directly embedded into a 1.5% agarose gel (Carl Roth GmbH + Co. KG) diluted in water.

Both paraffin- and agarose-embedded samples were first analysed by PBI. The paraffin-embedded samples were then sectioned in slices of 2 μm thickness, deparaffinized and pretreated. Tumor slices were further immunohistochemically stained with a monoclonal rabbit anti-human antibody against the epidermal growth factor receptor (EGFR) (Thermo Fisher Scientific MA5-16359, 1:500), as described by Saccomano *et al.* (2016), in order to detect tumor cells. Sections of mouse lungs were stained with a monoclonal rat anti-mouse cluster of differentiation 31 (CD31) (Dianova DIA-310, 1:10) antibody in order to label endothelial cells in vessels and capillaries.

Either Histofine Simple Stain MAX PO anti-rabbit (Nichirei, undiluted) or a biotin anti-rat antibody (BioLegend; 1:200) followed by avidin horseradish peroxidase (HRP) (eBioscience, 1:400) were used as secondary antibodies to assess the expression of the tumor marker EGFR and the capillary endothelial marker CD31, respectively. Furthermore, histochemical staining with hematoxylin eosin (H&E; Merck) and Masson trichrome (MT; Morphisto) was performed.

The agarose-embedded samples that were scanned by SRµCT were re-embedded in paraffin for further histological evaluation after the SRµCT scans, as described above.

2.4. SRµCT acquisition, phase retrieval and image quality assessment

Paraffin- and agarose-embedded samples were imaged by inline phase contrast CT using the white-beam setup of the SYRMEP beamline of the Italian synchrotron light source 'Elettra' with varying settings (summarized in Table 1):

(i) High-dose protocol: sample-to-detector distance SDD = 10 cm, 1800 angular projections, 2 s exposure time per projection, filter = 1 mm aluminium + 1 mm silica, leading to an average energy of 22 keV and a dose of $\sim$80 kGy.

(ii) Low-dose protocol: SDD = 10 cm, 900 angular projections, 50 ms exposure time per projection, filter = 1 mm silica (average energy 19 keV), dose $\sim$2 kGy.

The above-mentioned doses refer to the entrance dose at the sample position. The calculation is based on the values of fluxes emitted by the Elettra ring bending magnet and takes into consideration, for each energy bin, the tabulated flux-to-dose conversion factors. In addition, the calculations were confirmed by means of Monte Carlo simulations using *Fluka* code (http://www.fluka.org/).

In both protocols, the acquired data were directly streamed to a RAM disk. Therefore, the total acquisition time was 1 h for the high-dose and 45 s for the low-dose protocol.

The achieved voxel sizes were in the range 2–2.6 µm for a field of view (FOV) of $\sim$4–5.2 mm. Larger samples were scanned off-center over 360° which allowed almost doubling of the FOV.

For measuring the dependency of the CNR on the applied radiation dose and to demonstrate the advantage of using PBI, a PTA stained heart sample was subjected to multiple scans, consequently lowering the exposure time of the detector (1 s– 62.5 ms) while keeping all other parameters constant (900 angular projections, 1 mm silica filter and 10 cm SDD).

For phase retrieval, we used a single-distance phase-retrieval algorithm developed by Paganin *et al.* (2002) implemented within the SYRMEP tomo project (STP) software (Brun *et al.*, 2015), which requires the ratio of the real part (δ, describing the phase shift) and imaginary part (β, describing the absorption) of the complex refractive index, $n = 1 - \delta + i\beta$, to be constant. The application of this algorithm resulted in projection images that predominately display the phase shift properties within the sample. As a result of the dominant sample absorption, a low δ/β ratio of 100 was used for the phase-retrieval process. For image quality, the contrast-to-

noise ratio (CNR) between two materials (soft tissue and embedding material) was computed using the equation

$$CNR = \frac{\left|av(g_1) - av(g_2)\right|}{\left\{0.5\left[std(g_1)^2 + std(g_2)^2\right]\right\}^{1/2}} \quad (1)$$

as described by van Engen *et al.* (2006), where the parameters $av(g_1)$ and $std(g_1)$ denote the average and standard deviation of the grey values of a homogeneous area within the tissue, and $av(g_2)$ and $std(g_2)$ refer to the same parameters for the embedding material, respectively.

3. Results and discussion

3.1. Virtual SRµCT-based histology of differently stained paraffin-embedded soft-tissue specimens

In order to assess the pros and cons of the three different staining protocols, hearts, lungs, brains and xenograft pancreatic tumor tissue samples were explanted from mice, stained and embedded prior to analysis with PBI in combination with single-distance phase retrieval. A comparison of the staining protocols was performed on mouse tissue specimens that contained both lungs and hearts (Fig. 1):

(i) PTA staining of a mouse lung produced a strong contrast in the anatomical structures as illustrated in Fig. 1(*a*). Mainly the cartilage of the trachea, large bronchi and vessels were contrasted (Fig. 1*a*). A good visualization was also obtained for the epithelial cells of the alveoli.

Disadvantages of the PTA staining protocol were the long staining times and the generation of the strong X-ray absorption which resulted in the deposition of large radiation doses within the sample. Apart from the shrinkage caused by the dehydration process before paraffin embedding, no additional deformations of the samples were observed. The former is a well known phenomenon caused by the tissue processing steps utilized in standard histology (Zehbe *et al.*, 2010). Moreover, we demonstrated that PTA staining did not interfere with the subsequent application of IHC. Therefore, this approach can be integrated into the normal workflow of classical histological analysis as shown previously for heart tissue (Dullin *et al.*, 2017). A blackening of PTA stained samples in relation to the applied radiation dose was observed after SRµCT imaging which, however, resolved completely within 1–2 days for agarose-embedded and within 1–2 weeks for paraffin-embedded samples. Apart from this phenomenon, paraffin-embedded tissue samples scanned even multiple times (*e.g.* the heart sample in Fig. 2) did not show any dose-dependent tissue damage or quality impairment of the subsequent histological staining compared with unexposed regions of the samples.

(ii) I_2 staining requires a much shorter time to achieve complete penetration of mouse organs such as lung, heart and pancreas. Therefore, complete staining was reached in only a few hours, independent of the size and origin of the sample. As shown in Fig. 1(*b*), I_2 staining allowed the detailed depiction of

the alveolar lung structure and demonstrated a strong contrast of epithelial cells of the blood vessels and the bronchi. In addition, the bright staining of red blood cells allowed the distinction of blood vessels from the respiratory system. Therefore, this imaging approach has the major potential to depict alterations in these anatomical structures of the lung, especially in respiratory disease models. A similar imaging approach was used by Khonsari *et al.* (2014) to identify blood vessels within a mouse embryo.

It must be noted that I_2 staining resulted in a strong shrinkage of the samples, most probably resulting from the application of 100% ethanol in the I_2 staining solution.
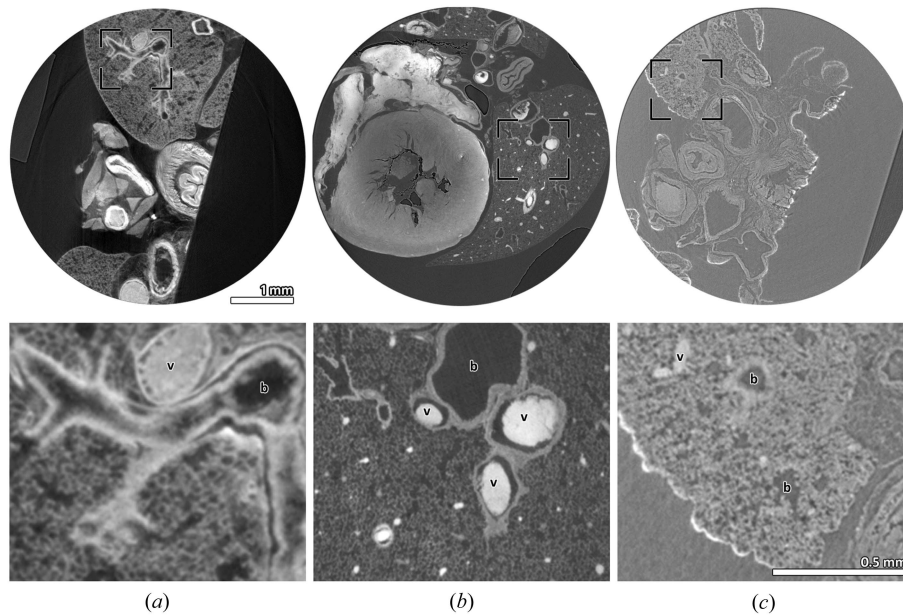

Figure 1
Comparison of SRµCT-based virtual histology of mouse lungs using three different staining protocols. Representative SRµCT scans of mouse lungs embedded in paraffin (voxel size = 2.6 µm) and stained with three different protocols (upper row): (*a*) PTA staining, (*b*) I_2 staining and (*c*) chrome alum staining. The detailed views (lower row) of the regions of interest (black squares) depicted in the overviews (upper row) show that all staining procedures allow a precise delineation of the lung parenchyma. In addition, scans of both PTA (*a*) and I_2 stained lungs (*b*) showed an increased contrast of bronchi (b) and vessel walls (v). In (*c*), only the blood within the vessels is highlighted (v). Note that in the I_2 stained sample, the blood is strongly stained allowing the differentiation between the vessel tree and the bronchial system of the respiratory tract.
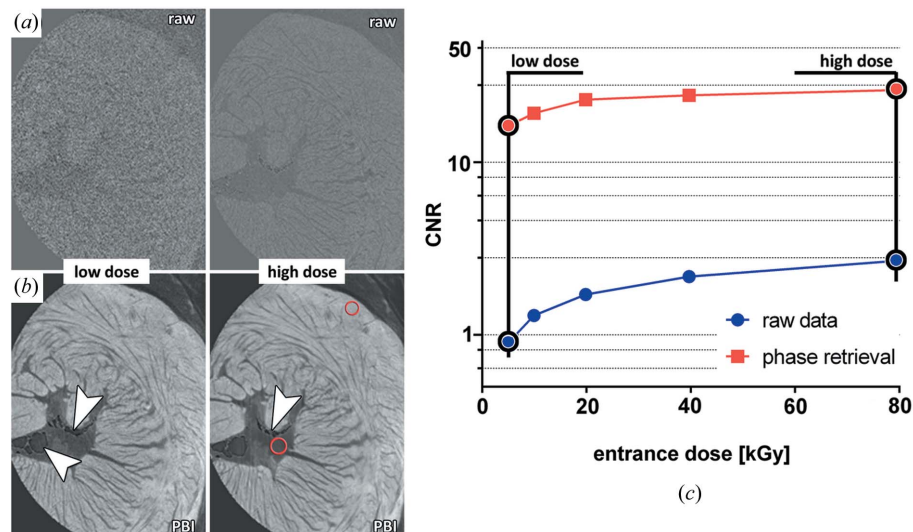

Figure 2
Relationship between radiation dose and CNR in CT scans of PTA stained mouse hearts embedded in paraffin. (*a*) Representative virtual slices of reconstructed raw data of a PTA stained paraffin embedded mouse heart, acquired at a low (5 kGy, left) and high (80 kGy, right) dose. (*b*) The same slices reconstructed after phase retrieval, resulting in reduced noise and a strong improvement of the image quality which depicts the anatomical structures of myocardial muscle fibers in more detail. In addition, dose-dependent crack formations in the paraffin are shown (white arrow heads). Note that the series of scans was started with high-dose scans, therefore the cracks appear larger at low dose. (*c*) By analyzing the CNR between heart muscle and paraffin [upper and lower red circle in (*b*), respectively] the phase-retrieved data (red curve) show around a tenfold increase in CNR at high dose and a less rapid decay at low dose than the reconstructed raw data. Note that at a dose of 5 kGy the CNR shows a 17-fold increase to the CNR of the reconstructed raw data (blue curve).

Table 2
Summary of the pros and cons of PTA, I$_2$ and chrome alum staining protocols.

	Phosphotungstic acid (PTA)	Iodine (I$_2$)	Chrome alum
Pros	Very good and intense tissue contrast Staining of red blood cells → visualization of vessels	Short staining times Staining of red blood cells → visualization of vessels	Short staining times
Cons	Long staining times especially for larger specimens	Tissue contrast not very strong Strong shrinkage of the samples	Faint tissue contrast (not compatible with classical µCT)

However, lowering the ethanol concentration can lead to inefficient staining as shown by Metscher *et al.* (2009*a,b*).

(iii) Chrome alum, which is usually used for staining of cell nuclei in histological analysis (Presnell *et al.*, 1997), produced a faint tissue contrast that proved to be insufficient for classical absorption-based µCT (data not shown). However, in combination with PBI, a low but overall clear delineation of the lung parenchyma was achieved (Fig. 1*c*) together with a slightly higher contrast within the blood vessels and bronchi. The advantage of chrome alum staining was twofold: a very short staining time and the complete removal of chrome alum during subsequent histological preparation of the tissue sample.

In summary, the three protocols resulted in a clear delineation of soft tissue within the lung. In particular, the PTA and I$_2$ staining protocols offered a strong soft-tissue contrast, which made these procedures suitable for classical µCT systems as demonstrated already by others in various applications (Metscher, 2009*a,b*; Silva *et al.*, 2015). Chrome alum staining may be especially beneficial in studies that analyze the biodistribution of radio-opaque nanoparticles as the anatomical structures can be visualized with a moderate contrast that does not overshadow the nanoparticles. Similar results were also obtained with the other organs. A summary of the main advantages and disadvantages of the three staining protocols considered is given in Table 2

3.2. Application of PBI on stained samples strongly improves image quality and allows for a lower radiation dose

In order to analyze the impact of PBI on image quality of SRµCT-based virtual histology in addition to reducing the radiation dose, a PTA stained and paraffin-embedded mouse heart was scanned multiple times, consequently lowering the detector exposure time. Data were reconstructed with and without the prior application of single-distance phase retrieval (Figs. 2*a*, 2*b*). CNR was measured within the selected regions of interest (ROIs) labelled in Fig. 2 (red circles) for a total of five sections.

At low dose, the image quality gained in the reconstructed phase-retrieved data (Fig. 2*b*) in comparison with the reconstructed raw data (Fig. 2*a*) is notably striking. Even for high-absorbing samples, like the presented PTA stained mouse heart embedded in paraffin, the use of PBI in combination with polychromatic X-rays enhanced the CNR dramatically by a factor of 10–17 depending on the applied radiation dose (Fig. 2*c*). Interestingly, the ratio between the CNR of the reconstructed raw data and phase-retrieved data increased at

lower radiation doses, indicating that PBI at low radiation doses is even more beneficial than at high doses (Fig. 2*c*). It is important to note that, although the selected ROI was chosen in a relatively homogeneous part of the tissue, the presence of different heart sub-structures increases the standard deviation and hence the estimated noise, leading to lower CNR values than expected.

Histological analysis revealed no tissue damage of the sample (even after multiple acquisitions). However, cracks in the paraffin formed as a result of high-dose scans. In the sample that was subjected to multiple acquisitions, the number of cracks increased from scan to scan [*e.g.* Fig. 2(*b*), white arrow head]. None of these substantially affected the image quality; however, they hampered subsequent cutting of histological sections as the whole paraffin block became brittle. By contrast, the application of the low-dose protocol did not introduce any damage or fractures into the specimen.

We found that both agarose- and paraffin-embedding procedures did not substantially affect the image quality in PBI. However, in terms of radiation sensitivity, gas bubbles formed within the agarose gel close to the surface of the tissue, especially in the high-absorbing PTA stained samples (data not shown), leading to a deformation of the object and artifacts in the reconstructed images.

3.3. µCT-based virtual histology provides a more reliable anatomical insight into soft tissue than classical histology

To verify whether the structures visualized by CT virtual histology correspond to the morphological structures obtained by microscopy of the histological sections, we compared the images obtained by both procedures on the same region of the tumor sample. An important advantage of CT imaging of paraffin-embedded samples was that no re-embedding was necessary before the cutting process, hence no additional deformation of the tissue specimen, besides the known cutting artifacts of a microtome, occurred. Thereby, this approach allowed for high precision in matching images of CT-based virtual histology with images of classic histology. Fig. 3(*a*) shows a microscope image of a 2 µm-thick tissue section of a PDAC tumor that developed in a nude mouse and was stained with an antibody against the tumor-associated antigen EGFR, known to be highly expressed in PDAC tumor cells (Saccomano *et al.*, 2016). The image contains a rupture of the embedded tissue (white arrow head), a typical sectioning artifact. The PBI three-dimensional data set of the same PDAC sample was cut virtually to display the identical anatomical region (Fig. 3*b*). The histological image and the
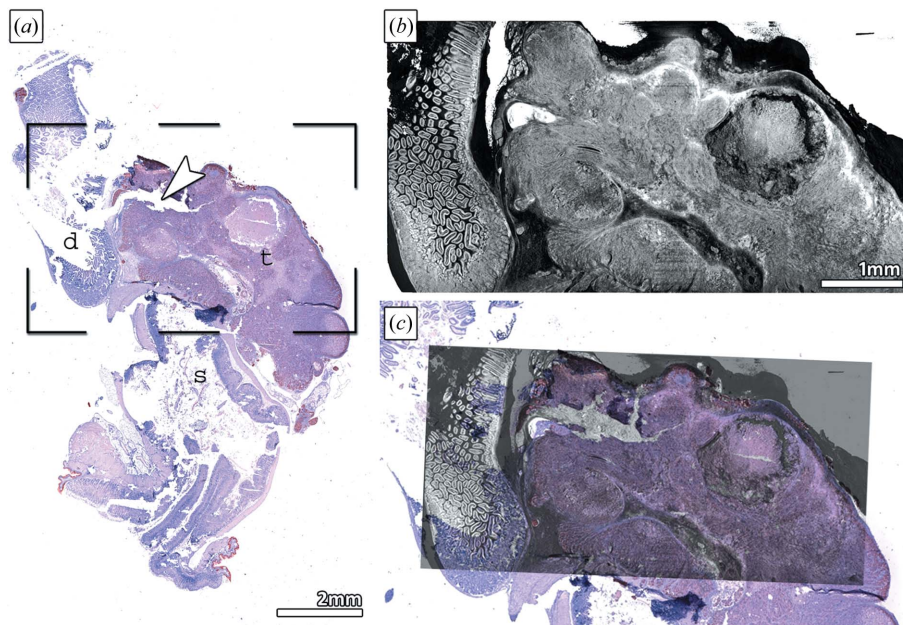
Figure 3
Overlay of classical histology and SRµCT-based virtual histology. (a) A microscope image of a human PDAC tumor established in a mouse by orthotopic transplantation of human AsPC-1 cells is shown. IHC with an anti-human-EGFR antibody identifies the tumor mass (t, light red color) developed in proximity of the stomach (s) and duodenum (d), both counterstained in violet by the H&E. Deformations and ruptures occurred during the cutting process, *i.e.* at the position indicated by the white arrow head. The ROI encasing the tumor mass was selected (black square). (b) Volume rendering of the ROI marked in (a) from a SRµCT scan (resolution 2.7 µm) of the entire AsPC-1 tumor sample embedded in paraffin together with stomach and duodenum. (c) Images of (a) and (b) were aligned to demonstrate the precise match of the same anatomical region imaged by SRµCT and by microscope, except for the ruptured region.

PBI data set could be precisely overlaid (despite the ruptured regions) proving that CT can visualize the same morphological structures of the tumor as microscopic analysis (Fig. 3c). Since CT-based virtual histology provides three-dimensional data sets without sectioning artifacts, precise measurements of anatomical structures can be performed easily and more reliably than by classical histology, especially in porous or fragile tissues. Currently, the main disadvantage of CT-based virtual histology is that, to date, no staining protocols exist for specific cell types. This method can therefore only supplement classical histology and IHC. For this reason, it is important that X-ray-based virtual histology does not interfere with subsequent histological analysis as demonstrated in Fig. S1 (see supporting information), where we show that H&E and MT staining as well as the IHC staining using an anti-CD31 antibody were successfully performed on a previously PTA stained and SRµCT-scanned lung sample.

3.4. SRµCT in combination with PBI enables virtual histology of unstained soft tissue

The presented staining approaches, particularly those using PTA and I$_2$, were originally developed to be used in combination with classical µCT (Metscher, 2009a,b; Silva *et al.*, 2015). Therefore, their purpose was to strongly increase the radio-opacity of the sample. As the distribution of the contrast is based on diffusion, tissue interfaces always appear blurry to a certain extent. In order to analyze the feasibility of virtual histology of unstained soft-tissue samples by exploiting the gain in image quality with PBI, we compared SRµCT scans of an unstained (Fig. 4a) and a PTA stained mouse brain (Fig. 4b) embedded in paraffin using the same acquisition parameters. Phase retrieval was applied with a δ/β ratio of 100. We found that the morphology of the cerebellum of the unstained brain (Fig. 4a) was visualized in more detail than the PTA stained brain (Fig. 4b) despite the overall lower contrast. This is shown in the insert of Fig. 4(a), which displays microscopic details of the three layers of the cerebellum of the unstained brain. Since both scans were acquired with the same settings (including the pixel size), we used the radially averaged power spectra of both images for comparison which is displayed in Fig. 4(c). The spectrum of the unstained brain (red curve) reveals reduced intensity in the low-frequency range and greater intensity in the high-frequency range compared with the PTA stained brain (black curve) pointing to a higher resolution. In addition, the power spectrum of the unstained brain shows a rapid decay at maximal frequency, suggesting a lower noise level than in the data set of the PTA stained brain. It must be noted that, without phase retrieval, the CT data of the unstained brain could not be visualized because of its low X-ray absorption (data not shown).

There is an intrinsic limitation of this approach that can be attributed to the single-distance phase-retrieval algorithm used, which requires a constant δ/β ratio within the samples, a ratio that depends on both energy and material. The chosen δ/β ratio of 100 can therefore not be optimal for both samples and was optimized for the unstained brain. To prove that the comparably lower image sharpness in the PTA stained
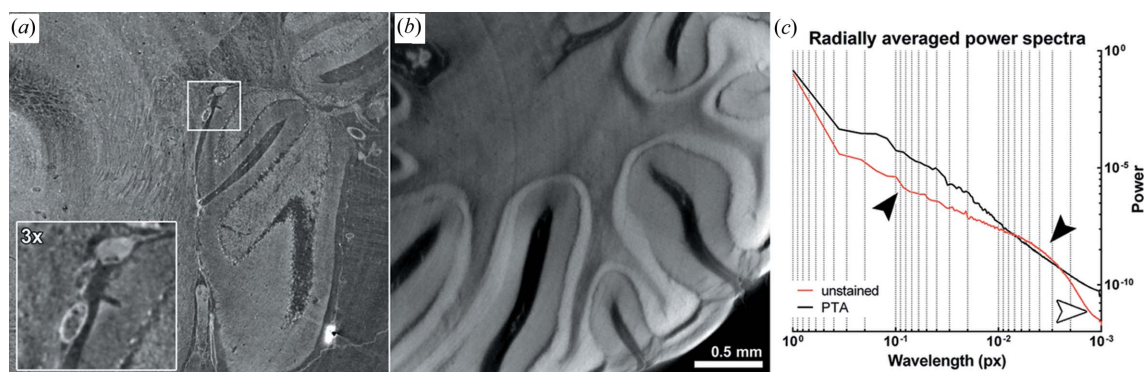
Figure 4
Comparison of SRµCT scans of an unstained and a PTA stained mouse brain embedded in paraffin: SRµCT scans of paraffin-embedded mouse brains, unstained (*a*) and PTA stained (*b*), and acquired with the same parameters, show a comparable area within the cerebellum. In (*a*) the structure of the cerebellum of the unstained brain is clearly distinguishable, especially in the detailed view (insert), demonstrating that the brain can be studied at cellular resolution. The different anatomical structures of the cerebellum of the PTA stained brain are also visualized in (*b*), but only at a limited level of detail in comparison with (*a*). (*c*) The radially averaged power spectra of the unstained brain data (red) show less content of low-frequency details and a higher content of high-frequency details (black arrow heads) than in the power spectrum of the PTA stained brain (black curve). In addition, the noise level is reduced in the unstained tissue as shown by the drop of the red curve for the smallest wavelengths (white arrow head).

specimen cannot be a result of a non-adequate δ/β ratio, we performed phase retrieval with various δ/β ratios [no-phase retrieval (0), 50, 100 and 200]. In Fig. S2(*a*), profile plots are shown at the position in the cerebellum indicated in Fig. S2(*b*), which illustrate that an edge enhancement can still be found by using a δ/β ratio of 100 [Fig. S2(*c*), arrow]. Therefore, the performed phase retrieval with a δ/β ratio of 100 cannot cause the observed lower degree of detail in the PTA stained samples, which must be therefore related to the diffusion process of the staining itself. Despite the fact that scanning of unstained soft tissue will remain a domain for phase-sensitive techniques only, it can be of great value in various biomedical applications as it will dramatically reduce the processing time of the tissue.

Phase contrast imaging of unstained tissue at higher energies might allow a further reduction of the applied dose because the contrast in PBI decreases less rapidly than in absorption-based imaging at higher energies.

Recent technical developments such as fine-focus X-ray tubes and/or the application of Fresnel lenses (Bidola *et al.*, 2017; Töpperwien *et al.*, 2017) allow the use of free-propagation-based phase contrast in X-ray microscopes (Wilkins *et al.*, 1996; Kitchen *et al.*, 2005). Thus, virtual X-ray-based histology of non-stained tissue can also be performed in laboratory-based systems as demonstrated previously (Dudak *et al.*, 2016; Bidola *et al.*, 2017; Kitchen *et al.*, 2005; Prajapati *et al.*, 2011), which will facilitate the dissemination of this label-free technique. However, as a result of the tremendous difference in X-ray flux, synchrotron sources will continue to outperform such systems, especially in terms of total acquisition time.

4. Conclusions

SRµCT allows high-precision virtual histology of stained soft-tissue samples and can be applied to paraffin- or agarose-embedded samples without interfering with the subsequent traditional processing protocol for classic histology and IHC.

The high radiation dose of polychromatic SRµCT, especially in combination with strong absorbing samples, does not damage the tissue itself; however, it affects the embedding material. If PBI is used in combination with single-distance phase-retrieval algorithms, a higher CNR can be achieved in combination with a lower radiation dose which prevents damage to the embedding material and enables the use of faint staining methods such as the presented chrome alum protocol. This might be especially suited for studies depicting the fate of nanoparticles as they are not overshadowed by a strongly stained background.

Moreover, PBI allows label-free virtual histology of unstained tissue, thus speeding up the entire approach. More importantly, if the intrinsic contrast of the tissue is used, a more detailed image can be obtained than from samples stained with a contrast agent. Therefore, we believe that SRµCT virtual histology of both stained and unstained soft-tissue samples presents a powerful tool for detailed morphological tissue analysis, supplementing classic histological techniques.

References

Bidola, P., Morgan, K., Willner, M., Fehringer, A., Allner, S., Prade, F., Pfeiffer, F. & Achterhold, K. (2017). *J. Microsc.* **266**, 211–220.

Brun, F., Pacilè, S., Accardo, A., Kourousias, G., Dreossi, D., Mancini, L., Tromba, G. & Pugliese, R. (2015). *Fundamenta Informaticae*, **141**, 233–243.

Clark, D. P. & Badea, C. T. (2014). *Phys. Med.* **30**, 619–634.

Duce, S., Morrison, F., Welten, M., Baggott, G. & Tickle, C. (2011). *Magn. Reson. Imaging*, **29**, 132–139.

Dudak, J., Zemlicka, J., Karch, J., Patzelt, M., Mrzilkova, J., Zach, P., Hermanova, Z., Kvacek, J. & Krejci, F. (2016). *Sci. Rep.* **6**, 30385.

Dullin, C., Ufartes, R., Larsson, E., Martin, S., Lazzarini, M., Tromba, G., Missbach-Guentner, J., Pinkert-Leetsch, D., Katschinski, D. M. & Alves, F. (2017). *PLoS One*, **12**, e0170597.

Handschuh, S., Schwaha, T. & Metscher, B. D. (2010). *BMC Dev. Biol.* **10**, 41.

Johnson, J. T., Hansen, M. S., Wu, I., Healy, L. J., Johnson, C. R., Jones, G. M., Capecchi, M. R. & Keller, C. (2006). *PLoS Genet.* **2**, e61.

Khonsari, R. H., Healy, C., Ohazama, A., Sharpe, P. T., Dutel, H., Charles, C., Viriot, L. & Tafforeau, P. (2014). *Anat. Rec. Hoboken NJ 2007*, **297**, 1803–1807.

Kienan, J. A. (2008). *Histological and Histochemical Methods: Theory and Practice*. Banbury: Scion Publishing Ltd.

Kitchen, M. J., Lewis, R. A., Yagi, N., Uesugi, K., Paganin, D., Hooper, S. B., Adams, G., Jureczek, S., Singh, J., Christensen, C. R., Hufton, A. P., Hall, C. J., Cheung, K. C. & Pavlov, K. M. (2005). *Br. J. Radiol.* **78**, 1018–1027.

Li, X., Liu, J., Davey, M., Duce, S., Jaberi, N., Liu, G., Davidson, G., Tenent, S., Mahood, R., Brown, P., Cunningham, C., Bain, A., Beattie, K., McDonald, L., Schmidt, K., Towers, M., Tickle, C. & Chudek, S. (2007). *J. Anat.* **211**, 798–809.

Liu, X. S., Zhang, X. H., Rajapakse, C. S., Wald, M. J., Magland, J., Sekhon, K. K., Adam, M. F., Sajda, P., Wehrli, F. W. & Guo, X. E. (2010). *J. Bone Miner. Res.* **25**, 2039–2050.

Masyuk, T. V., Ritman, E. L. & LaRusso, N. F. (2001). *Am. J. Pathol.* **158**, 2079–2088.

Metscher, B. D. (2009a). *BMC Physiol.* **9**, 11.

Metscher, B. D. (2009b). *Dev. Dyn.* **238**, 632–640.

Missbach-Guentner, J., Pinkert-Leetsch, D., Dullin, C., Ufartes, R., Hornung, D., Tampe, B., Zeisberg, M. & Alves, F. (2018). *Sci. Rep.* **8**, 1407.

Mohammadi, S., Larsson, E., Alves, F., Dal Monego, S., Biffi, S., Garrovo, C., Lorenzon, A., Tromba, G. & Dullin, C. (2014). *J. Synchrotron Rad.* **21**, 784–789.

Ourselin, S., Bardinet, E., Dormont, D., Malandain, G., Roche, A., Ayache, N., Tandé, D., Parain, K. & Yelnik, J. (2001). *Medical Image Computing and Computer-Assisted Intervention (MICCAI 2001)*, pp. 743–751. Berlin: Springer.

Paganin, D., Mayo, S. C., Gureyev, T. E., Miller, P. R. & Wilkins, S. W. (2002). *J. Microsc.* **206**, 33–40.

Prajapati, S. I., Kilcoyne, A., Samano, A. K., Green, D. P., McCarthy, S. D., Blackman, B. A., Brady, M. M., Zarzabal, L. A., Tatiparthy, A. K., Sledz, T. J., Duong, T., Ohshima-Hosoyama, S., Giles, F. J., Michalek, J. E., Rubin, B. P. & Keller, C. (2011). *Mol. Imaging Biol.* **13**, 493–499.

Presnell, S. C., Stolz, D. B., Mars, W. M., Jo, M., Michalopoulos, G. K. & Strom, S. C. (1997). *Mol. Carcinog.* **18**, 244–255.

Saccomano, M., Dullin, C., Alves, F. & Napp, J. (2016). *Int. J. Cancer*, **139**, 2277–2289.

Schulz, G., Weitkamp, T., Zanette, I., Pfeiffer, F., Beckmann, F., David, C., Rutishauser, S., Reznikova, E. & Müller, B. (2010). *J. R. Soc. Interface*, **7**, 1665–1676.

Souza e Silva, J. M. de, Zanette, I., Noël, P. B., Cardoso, M. B., Kimm, M. A. & Pfeiffer, F. (2015). *Sci. Rep.* **5**, 14088.

Tomer, R., Lovett-Barron, M., Kauvar, I., Andalman, A., Burns, V. M., Sankaran, S., Grosenick, L., Broxton, M., Yang, S. & Deisseroth, K. (2015). *Cell*, **163**, 1796–1806.

Töpperwien, M., Krenkel, M., Vincenz, D., Stöber, F., Oelschlegel, A. M., Goldschmidt, J. & Salditt, T. (2017). *Sci. Rep.* **7**, 42847.

Van Engen, R., Young, K., Bosmans, H. & Thijssen, M. (2006). *European Guidelines for Quality Assurance in Breast Cancer Screening and Diagnosis: Fourth Edition, Supplements.*, Vol. 1, pp. 105–150.

Wilkins, S. W., Gureyev, T. E., Gao, D., Pogany, A. & Stevenson, A. W. (1996). *Nature (London)*, **384**, 335–338.

Zehbe, R., Haibel, A., Riesemeier, H., Gross, U., Kirkpatrick, C. J., Schubert, H. & Brochhausen, C. (2010). *J. R. Soc. Interface*, **7**, 49–59.